Evidence of bicluster structure in the ground state of ^{20}Ne

Y. Yamaguchi [1], W. Horiuchi [1,2,3,4,*] and N. Itagaki [1,2,3,†]

[1]*Department of Physics, Osaka Metropolitan University, Osaka 558-8585, Japan*
[2]*Nambu Yoichiro Institute of Theoretical and Experimental Physics (NITEP), Osaka Metropolitan University, Osaka 558-8585, Japan*
[3]*RIKEN Nishina Center, Wako 351-0198, Japan*
[4]*Department of Physics, Hokkaido University, Sapporo 060-0810, Japan*

(Received 16 May 2023; accepted 20 June 2023; published 21 July 2023)

We explore the structure of the ground state of ^{20}Ne by investigating various density profiles. Four candidates for the ground state configurations, (a) j-j coupling and (b) SU(3) shell model and (c) 5α and (d) ^{16}O+α cluster model configurations, are generated by utilizing the antisymmetrized quasicluster model. A high-energy reaction theory, the Glauber model, relates these one-body density distributions and reaction observables. The angular distributions of the elastic scattering cross sections clearly distinguish these configurations and tell which is the most plausible one: The ground state of ^{20}Ne favors a 16 + 4 nucleon bicluster structure. A comprehensive investigation of other electric observables also supports this conclusion.

DOI: 10.1103/PhysRevC.108.014322

I. INTRODUCTION

Nuclear clustering phenomena often appear in light $N = Z$ nuclei [1–4]. Accounting for the α (^{4}He) clustering is essential to understand their low-lying states. Especially, the first excited $J^\pi = 0^+$ states play an important role in explaining nucleosynthesis producing ^{12}C and ^{16}O elements [5,6] and they are well explained by 3α [7] and ^{12}C+α [8,9] cluster models, respectively. See Ref. [3] for a comprehensive review of these α clustered nuclei. Clustering phenomena are closely related to the bosonic property of the nuclear system. Ref. [10] proposed that some multi-α states can be interpreted as a Bose-Einstein condensed state. Experimental searches for the α condensed states have been made for ^{16}O [11] and ^{20}Ne [12].

Quantifying the degree of nuclear clustering is one of the hot topics in nuclear physics. An analysis of the α knockout reaction for ^{20}Ne was performed, and the degree of the ^{16}O+α cluster structure was quantified [13]. The α clustering is also found in the surface region of heavy nuclei such as Sn isotopes [14]. Recently, two of the present authors (W.H. and N.I.) developed an efficient way to visualize the ground state structure by using the proton-nucleus elastic scattering combined with the antisymmetrized quasicluster model (AQCM) [15,16]. The shell and cluster configurations can easily be distinguished in comparison with angular distributions of the cross sections at the first diffraction peak.

It should be noted that the ground state structure of ^{20}Ne is still controversial and we need comprehensive understanding. The structure of ^{20}Ne has been recognized as having ^{16}O+α structure, which explains positive and negative parity rotational bands, the so-called inversion doublet [3,17]. The 5α cluster model calculation showed that the most probable ground state structure is the ^{16}O+α bicluster structure [18]. On the other hand, the nonclustered rotational model can also reproduce the electric properties of the low-lying states of ^{20}Ne [19–21]. A fully microscopic description of ^{20}Ne suggested that the coexistence of deformed mean-field and cluster pictures in the low-lying spectrum of ^{20}Ne [22–25].

Furthermore, in Ref. [16], the AQCM analysis was applied to ^{16}O and concluded that the structure of the ground state has most likely 4α tetrahedron configuration in line with modern *ab initio* calculations [26]. One may ask a question: If this interpretation is accepted, the ground-state structure of ^{20}Ne could have 5α structure, while ^{20}Ne structure has been recognized as the p-shell closed ^{16}O plus α structure. There is a need to clarify the most probable structure of ^{20}Ne using different observables.

In this paper, we perform the AQCM analysis to unveil the ground state structure of ^{20}Ne. The density profiles generated from different AQCM configurations are investigated by using proton-nucleus elastic scattering. We also compute other observables and compare them with experimental data to see more details about the density distributions.

In the next section, we explain the theoretical framework used in this study. The ^{20}Ne wave function with the AQCM is defined. The evaluation of the one-body density distribution is explained, which is used as an input to the high-energy reaction theory, the Glauber model. Section III explains how we generate various AQCM configurations in detail. We discuss the properties and density profiles of the four specific configurations. Using these one-body density distributions, the proton-^{20}Ne elastic scattering cross sections and elastic charge form factors are computed and compared with available experimental data. The conclusion is made in Sec. IV.

*whoriuchi@omu.ac.jp
†itagaki@omu.ac.jp

II. METHOD

A. Configurations of ^{20}Ne with antisymmetrized quasicluster model

The configurations of ^{20}Ne are generated by the antisymmetrized quasicluster model (AQCM) [27–40]. The AQCM is an extension of the multi-α cluster model [41], which allows one to express not only cluster model but also the j-j coupling and SU(3) shell model configurations in a single scheme. The AQCM basis state for ^{20}Ne is expressed by the 5α cluster model as

$$\Phi(\nu, d, d_5, \Lambda) = \mathcal{A}\left\{\prod_{i=1}^{5} \Phi_\alpha(\nu, R_i, \Lambda)\right\}, \tag{1}$$

where $\mathcal{A}$ is the antisymmetrizer for nucleons. Here, $\Phi_\alpha(\nu, R_i, \Lambda)$ is the ith α particle wave functions with the Gaussian center parameter $\boldsymbol{R}_i$ defined by

$$\Phi_\alpha(\nu, R_i, \Lambda) = \phi_1^\nu(\uparrow, p)\phi_2^\nu(\downarrow, p)\phi_3^\nu(\uparrow, n)\phi_4^\nu(\downarrow, n) \tag{2}$$

with a single-nucleon Gaussian wave packet with spin χ_s ($s = \uparrow$ or $\downarrow$) and isospin η_t ($t = p$ or n) wave functions

$$\phi_j^\nu(s, t) = \left(\frac{2\nu}{\pi}\right)^{3/4} \exp[-\nu(\boldsymbol{r}_j - \boldsymbol{\zeta}_i)^2]\chi_s\eta_t, \tag{3}$$

where

$$\boldsymbol{\zeta}_i = \boldsymbol{R}_i + i\Lambda\boldsymbol{e}^{\rm spin} \times \boldsymbol{R}_i \tag{4}$$

with $\boldsymbol{e}^{\rm spin}$ being a unit vector for the intrinsic-spin orientation of a nucleon. Note that the AQCM basis state with $\Lambda = 0$ is nothing but the Brink model [41], where the spin-saturated α cluster is assumed and no contribution from the spin-orbit interaction is realized. To express the independent particle motion with a good total angular momentum j, the imaginary part of the Gaussian center parameter is introduced in the AQCM.

The basis function of ^{20}Ne is expressed by the four-α part and the additional fifth α wave function. In the four-α part, the four α particles are placed at vertexes of a tetrahedron with a common inter-α-cluster distance $d = |\boldsymbol{R}_i - \boldsymbol{R}_j|$ ($i \neq j \leqslant 4$). Note that one can obtain the p-shell closure configuration $(0s)^4(0p)^{12}$ for ^{16}O with a limit of $d \to 0$ [41] independent of a choice of Λ. Here, we place the fifth α particle along the z axis passing through the center of the bottom face of the tetrahedron. The distance between the fifth α particle and the center of the tetrahedron is denoted as d_5. With this geometry of the α particles, one can obtain both the SU(3) $[(0s)^4(0p)^{12}(1s0d)^4]$ and the j-j coupling $[(0s)^4(0p)^{12}(0d_{5/2})^4]$ shell model configurations by taking $\Lambda = 0$ and 1, respectively, in the limit of $d, d_5 \to 0$ [30].

Once the parameters of the AQCM basis function, i.e., ν, d, d_5, and Λ, are fixed, we can compute the nucleon one-body density distribution in the body-fixed frame with the mass number A as

$$\tilde{\rho}(\boldsymbol{r}) = \langle\Phi|\sum_{i=1}^{A}\delta(\boldsymbol{r}_i - \boldsymbol{r})|\Phi\rangle/\langle\Phi|\Phi\rangle. \tag{5}$$

Note $\sum_{i=1}^{A}\langle\Phi|\boldsymbol{r}_i|\Phi\rangle = 0$. $\tilde{\rho}$ in general includes the center-of-mass motion. This is properly removed by using the prescription given by Ref. [42]:

$$\int d\boldsymbol{r}\, e^{i\boldsymbol{k}\cdot\boldsymbol{r}}\rho_{\rm int}(\boldsymbol{r}) = \exp\left(\frac{k^2}{8A\nu}\right)\int d\boldsymbol{r}\, e^{i\boldsymbol{k}\cdot\boldsymbol{r}}\tilde{\rho}(\boldsymbol{r}). \tag{6}$$

The density distribution in the laboratory frame is obtained by averaging the center-of-mass-free density distribution in the body-fixed frame over angles as [43]

$$\rho(r) = \frac{1}{4\pi}\int d\hat{\boldsymbol{r}}\,\rho_{\rm int}(\boldsymbol{r}). \tag{7}$$

B. High-energy reaction observables

To relate the density profile to the reaction observables, we calculate the elastic scattering and total reaction cross sections using a high-energy microscopic reaction theory, the Glauber model [44]. Here, we briefly explain how to get the cross sections with the one-body density distribution obtained above.

The scattering amplitude of the proton-nucleus elastic scattering is given by [45]

$$f(\theta) = F_C(\theta) + \frac{ik}{2\pi}\int d\boldsymbol{b}\, e^{-i\boldsymbol{q}\cdot\boldsymbol{b}+2i\eta\ln(kb)}\left(1 - e^{i\chi_{pT}(\boldsymbol{b})}\right), \tag{8}$$

where $F_C(\theta)$ is the Rutherford scattering amplitude, $\boldsymbol{b}$ is the impact parameter vector, and η is the Sommerfeld parameter. The relativistic kinematics is used for the wave number k. With this scattering amplitude, the proton-nucleus elastic scattering differential cross section is computed by

$$\frac{d\sigma}{d\Omega} = |f(\theta)|^2. \tag{9}$$

The optical phase-shift function χ_{pT} in the optical-limit approximation (OLA) is given by [44,45]

$$i\chi_{pT}(\boldsymbol{b}) \approx -\int d\boldsymbol{r}\,[\rho_p(\boldsymbol{r})\Gamma_{pp}(\boldsymbol{b} - \boldsymbol{s}) + \rho_n(\boldsymbol{r})\Gamma_{pn}(\boldsymbol{b} - \boldsymbol{s})], \tag{10}$$

where $\boldsymbol{r} = (\boldsymbol{s}, z)$ is the single-nucleon coordinate measured from the center of mass coordinate of the projectile nucleus with z being the beam direction. The inputs to the theory are the density distribution obtained by Eq. (7) and proton-proton (proton-neutron) profile function Γ_{pp} (Γ_{pn}), which is often parametrized as [46]

$$\Gamma_{NN}(\boldsymbol{b}) = \frac{1 - i\alpha_{NN}}{4\pi\beta_{NN}}\sigma_{NN}^{\rm tot}e^{-\frac{b^2}{2\beta_{NN}}} \tag{11}$$

for each incident energy. The parameter sets of α_{NN}, β_{NN}, and $\sigma_{NN}^{\rm tot}$ are given in Ref. [47], which are well tested for proton-nucleus scattering [15,16,21,48,49]. As discussed in Ref. [50], the proton-elastic scattering has a strong sensitivity to the density profiles near the nuclear surface and can be used as a spectroscopic tool to distinguish shell and cluster configurations in light- to medium-mass nuclei [15,16].

The total reaction cross sections offer direct observables of nuclear size properties and are used to verify our wave function in the present study. In the Glauber model [44], σ_R

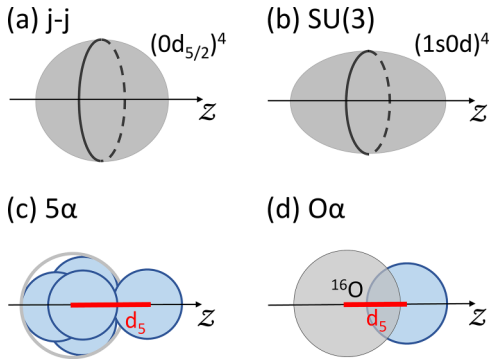

FIG. 1. Schematic illustration of adopted configurations of ^{20}Ne. (a) j-j coupling and (b) SU(3) shell model configurations and (c) 5α and (d) bicluster (Oα) configurations. Sizes of α and ^{16}O clusters and their distance are drawn, reflecting the actual scales given in Table I.

is calculated by

$$\sigma_R = \int d\boldsymbol{b}\left(1 - |e^{i\chi_{PT}(\boldsymbol{b})}|^2\right). \tag{12}$$

Here, we employ the nucleon-target formalism in the Glauber model (NTG) [51] to evaluate projectile-target optical phase-shift function $\chi_{PT}(\boldsymbol{b})$, which only requires the one-body density distributions of the projectile and target nuclei and the profile function. We investigate σ_R on a carbon target, in which the experimental data are available. The harmonic-oscillator-type density that reproduces the charge radius is employed for the carbon target. It is known that a carbon target has strong sensitivity to the density profiles near the nuclear surface [52,53]. We remark that the present reaction model has been used as a standard tool for extracting nuclear size properties from the interaction cross section measurements [54–56] as it works well shown in many examples of the nucleus-nucleus scattering [42,43,48,57–60].

III. RESULTS

A. Properties of ^{20}Ne configurations

In this paper, we examine four types of density profiles of ^{20}Ne obtained from the AQCM basis functions with proper choices of ν, d, d_5, and Λ, extending the direction made in Refs. [15,16]. We set all these generated AQCM configurations to reproduce the measured charge radius of ^{20}Ne [61]. The schematic pictures of these four configurations are illustrated in Fig. 1 and their details are described below.

First, we consider two types of shell-model configurations, j-j coupling and SU(3) shell models, illustrated in panels (a) and (b) of Fig. 1, corresponding to $(0d_{5/2})^4$ and $(1s0d)^4$ configurations, respectively. In the AQCM, the j-j [SU(3)] configuration can be expressed taking $\Lambda = 1$ ($\Lambda = 0$) in a limit of $d, d_5 \to 0$. The remaining oscillator parameter ν is fixed to reproduce the measured charge radius of ^{20}Ne [61]. Hereafter, they are called j-j and SU(3) configurations, respectively. The latter corresponds to the axially symmetric harmonic oscillator model, which exhibits prolate deformation.

TABLE I. Properties of the four specific AQCM configurations of ^{20}Ne. Values in parentheses are obtained with the ideal shell-model configurations. See text for details. All the root-mean-square point-proton radii of these configurations are commonly set to 2.89 fm [61].

	ν (fm^{-2})	d (fm)	d_5 (fm)	Λ	$\langle Q\rangle$	$\langle LS\rangle$	$\langle P\rangle$
j-j	0.1453	0.001	0.01	1	20.0(20)	3.99(4)	−4.0(−4)
SU(3)	0.1453	0.001	0.01	0	20.0(20)	0.00(0)	−4.0(−4)
5α	0.2656	3.058	3.895	0	32.3	0.00(0)	−1.5
Oα	0.1635	0.001	3.012	0	21.3	0.00(0)	−3.7

Next, two types of cluster-model configurations are prepared. The 5α configuration is generated by taking into account the 4α tetrahedron structure of ^{16}O [16]. As illustrated in panel (c), in the AQCM, a 5α-like cluster configuration is expressed by taking the ν parameter of the free α particle and the d value reproducing the charge radius of ^{16}O with $\Lambda = 0$ [16]. Then the distance of the fifth α particle, d_5, is set to reproduce the measured charge radius of ^{20}Ne. This is called 5α configuration.

Another cluster configuration represents a bicluster or ^{16}O +α like clustering, which divides 20 nucleons into 16 + 4 nucleons drawn in panel (d) of Fig. 1. The 4α part is constructed based on the p-shell closed shell model configuration, which can be realized in the AQCM by taking $d \to 0$ with ν reproducing the charge radius of ^{16}O [16], and then the d_5 value is fixed to reproduce the measured charge radius of ^{20}Ne. Hereafter, this is called Oα or bicluster configuration.

Table I lists the thus-obtained AQCM parameter sets, and calculated nuclear properties with these four configurations of ^{20}Ne: the total harmonic oscillator quanta $\langle Q\rangle$, the expectation values of single-particle spin-orbit operators $\sum_{i=1}^{A} \boldsymbol{l}_i \cdot \boldsymbol{s}_i$, $\langle LS\rangle$, and the single-particle parity operators $\sum_{i=1}^{A} P_i$ with $P_i f(\boldsymbol{r}_i) = f(-\boldsymbol{r}_i)$, $\langle P\rangle$. We confirm that the $\langle Q\rangle$, $\langle LS\rangle$, and $\langle P\rangle$ values of the shell model configurations reproduce the expected values from the j-j and SU(3) shell model configurations given in parentheses.

Both the cluster configurations, 5α and Oα types, exhibit large d_5 values, about 3–4 fm, indicating a well-developed cluster structure: The d and d_5 values are comparable in the 5α configuration, representing a trigonal bipyramid configuration. In the Oα configuration, the large d_5 value of 3.01 fm is found, which is comparable to the sum of the matter radii of the p-shell closed ^{16}O and four-nucleon cluster, 2.57 and 1.85 fm, respectively, indicating well developed 16 + 4 bicluster structure.

The 5α configuration predict the largest $\langle Q\rangle$ value, while the Oα configuration shows slightly larger $\langle Q\rangle$ value compared to the ideal shell model configuration, $\langle Q\rangle = 20$. This is because, in the 5α configuration, the 4α configuration in ^{16}O core already includes high oscillator quanta as $\langle Q\rangle = 18.6$ originating from the large intercluster distances when the ν value is large [16]. This happens in general when a nuclear system exhibits well-developed cluster structure [8,9,62–65]. As the charge radius of ^{20}Ne is larger than that of ^{16}O, the additional fifth α particle should be located at the surface region of ^{16}O, resulting in high $\langle Q\rangle$ value. In contrast, for

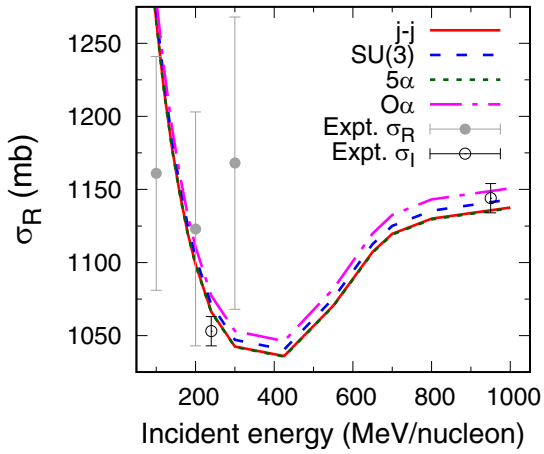

FIG. 2. Total reaction cross sections on a carbon target of ^{20}Ne as a function of incident energy. The experimental total reaction (σ_R) and interaction cross section (σ_I) data are taken from Refs. [66–68].

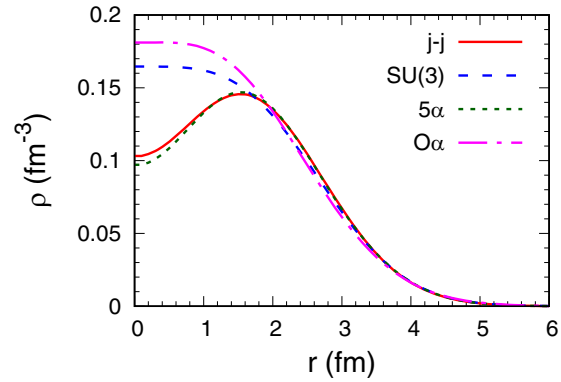

FIG. 3. Nucleon density distributions of ^{20}Ne with the four types of configurations. See text for details.

the Oα configuration, since the ν value is much smaller than that of the free α particle, the mixing of higher major shell components is suppressed.

To verify those four configurations, we calculate the total reaction cross sections on a carbon target using the density distributions obtained from these four configurations. Figure 2 plots the calculated total reaction cross sections on a carbon target as a function of incident energy. The experimental total reaction (σ_R) and interaction (σ_I) cross section data are also plotted for comparison. The uncertainties of the σ_R data are quite large and do not help constrain the theoretical results in the present paper. The calculated σ_R results reasonably reproduce the experimental σ_I data, considering that the difference between σ_R and σ_I is tens of mb [69] and the difference becomes larger in general, as the incident energy decreases [21]. Noting that $\sigma_R > \sigma_I$ always holds, the Oα configurations give the best reproduction of the data. However, the experimental uncertainties of σ_I are comparable to the differences in the total reaction cross sections calculated with the four density profiles. Other observables should be investigated to conclude which configurations are the most probable in ^{20}Ne.

B. Density profiles of ^{20}Ne

The characteristics of these four configurations can be seen in the density profiles. Figure 3 plots the one-body density distributions of ^{20}Ne. The j-j and 5α configurations exhibit the so-called "bubble" structure, while the central depressions are filled in the SU(3) and Oα configurations. The nature of the bubble structure is the lack of occupation of the s orbit. The bubble structure of the j-j configuration is simply understood by $(0s)^4(0p)^{12}(0d_{5/2})^4$ configuration, where the $1s$ orbit is absent. For the 5α configuration, the bubble structure is developed as the additional fifth α particle is located at the surface of the ^{16}O cluster and the 4α configurations of ^{16}O part already have the bubble structure [16]. For the SU(3) and Oα-cluster configurations, the fifth α cluster should occupy the sd shell and the central depression disappears by the occupation of the s orbit. This can also be interpreted as the deformation effect which induces the configuration mixing of the single-particle orbits near the Fermi level [70]. We remark that the recent no-core shell model calculation predicts the $(\lambda, \mu) = (N_z - N_x, N_x - N_y) = (8, 0)$ dominance in the ground state of ^{20}Ne [71], where N_k is the oscillator quanta of the k $(= x, y, z)$ direction. This $(\lambda, \mu) = (8, 0)$ configuration corresponds the SU(3) configuration in the present paper, showing nonbubble structure. Note that the Oα configuration is expressed by a superposition of $(\lambda, 0)$ configurations whose occupation numbers depend on the intercluster distance. As we see later, the Oα configuration includes a large component of the SU(3) configuration.

In most cases, the nuclear deformation diffuses the density profiles near the nuclear surface compared to the spherical limit. It is convenient to quantify the density profile near the nuclear surface. For this purpose, we evaluate the diffuseness parameter of the one-body density distribution using the prescription given in Ref. [50], where a two-parameter Fermi (2pF) function,

$$\rho_{\rm 2pF}(\bar{R}, a, r) = \frac{\rho_0}{1 + \exp[(r - \bar{R})/a]}, \tag{13}$$

is determined by the least square method by minimizing

$$\int_0^\infty dr\, r^2 \left|\rho_{\rm 2pF}(\bar{R}, a, r) - \rho(r)\right|. \tag{14}$$

for the radius $\bar{R}$ and diffuseness a parameters. ρ_0 is determined by the normalization condition. Note that the obtained a parameter can be extracted accurately from the proton-nucleus elastic scattering cross section measurement up to the first diffraction peak [50]. Many examples [50,72–78] showed that the nuclear diffuseness can be used to deduce the spectroscopic properties of various nuclear systems.

The calculated diffuseness parameters are 0.501, 0.544, 0.507, and 0.585 fm for the j-j, SU(3), 5α, and Oα configurations, respectively. We note that the a value becomes large when the nodal low angular momentum states, i.e., $1s$ orbit, are occupied [77], while it becomes small in the bubble nuclei [72]. The calculated diffuseness clearly reflects the information on the nuclear surface showing large a values for

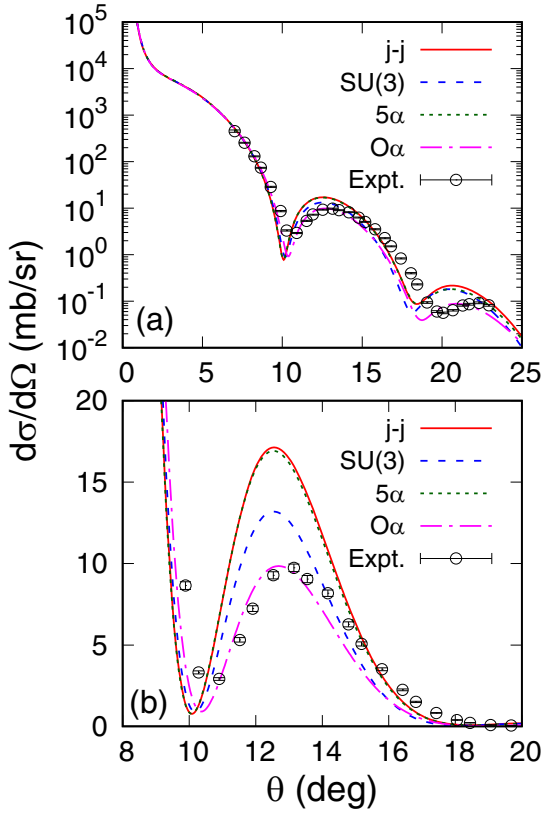

FIG. 4. Proton-nucleus differential elastic scattering cross sections for ^{20}Ne at incident energies of 800 MeV as a function of scattering angles in (a) logarithmic and (b) linear scales. The experimental data are taken from Ref. [79].

the SU(3) and Oα configurations, where the occupation of the 1s orbit is significant.

C. Ground-state structure of ^{20}Ne

Those four different density profiles can be distinguished by the proton-nucleus elastic scattering [15,16]. Figure 4 compares the differential cross sections for the proton-^{20}Ne elastic scattering. Incident proton energy is chosen to 800 MeV, where the experimental data are available. The cross sections in logarithmic and linear scales are plotted. As we see in the figure, the differences between those four configurations are apparent. The bicluster configuration is best for reproducing the data, explaining the available data up to the second peak position.

The 5α and j-j coupling shell model configurations significantly overestimate the experimental data. The sharper the nuclear surface, the larger the cross sections at the first peak position become [50]. In fact, these configurations give significantly smaller a values compared to the others as were given in the previous subsection. For the 5α configuration, because "sharp" five α particles are located near the nuclear surface, the cross sections near the first diffraction peak are enhanced compared to the Oα configuration. As the j-j type has no 1s components, the nuclear surface becomes sharp with the occupancy of the higher angular momentum state, i.e., $0d_{5/2}$ orbit [72]. The SU(3) shell model configuration shows intermediate between the bubble and bicluster density profiles. This can be explained by investigating the degree of nuclear deformation.

As a measure of the nuclear quadrupole deformation, we calculate the reduced quadrupole transition probabilities from $J^\pi = 2^+$ to the ground 0^+ states [$B(E2\downarrow)$] by using parity and angular momentum projected intrinsic wave functions Φ for each configuration as in Ref. [23]. The calculated $B(E2)$ values are 6.42, 18.8, 51.0, and 41.9 e^2fm^4 for j-j, SU(3), 5α, and Oα types, respectively. As expected, the j-j coupling configuration gives the smallest $B(E2)$ value. These for the cluster type configurations are large and comparable to the experimental data, $56.0 \pm 8.0\, e^2$fm^4 [80,81]. The value for the SU(3) configuration is approximately half of these clustered configurations. Though the one-body density of the SU(3) configuration has a diffused nuclear surface due to the mixture of the 1s orbit, the present SU(3) shell model configuration has a less deformed shape, which is not enough to explain the elastic scattering cross sections at the first peak position.

The proton-elastic scattering has of particular sensitivity to the density profiles near the nuclear surface [50]. For a more detailed understanding of the structure of ^{20}Ne, we evaluate the elastic charge form factor, which has traditionally been investigated as a direct observable of the nuclear charge distribution using electron scattering [82]. Since the electron-nucleus interaction is weaker than that of the proton-nucleus one, the electron scattering can probe more internal regions of the charge density distribution than the proton scattering. The elastic charge form factor is evaluated by the Fourier transform of the density distribution with the convolution of the finite proton charge as [7,16]

$$|F(q)|^2 = \left|\frac{1}{A}\int_0^\infty dr\, \rho(r) j_0(qr) r^2\right|^2 \exp\left(-\frac{1}{2}a_p^2 q^2\right) \quad (15)$$

with $a_p^2 = 0.514$ fm^2, which reproduces the charge radius of a proton, 0.878 fm [61].

Figure 5(a) displays the square of the elastic charge form factors of ^{20}Ne as a function of the momentum transfer. The Coulomb distortion effect on the momentum transfer is taken into account in the experimental data [19,83]. For the sake of visibility, we also draw it for low-momentum transfer region in panel (b). We see that the Oα configuration perfectly reproduces the form factors up to $q \approx 1.4$ fm^{-1} but it fails to reproduce the data at higher q, while the j-j and 5α configurations reproduce the high q data. This suggests that the wave function of ^{20}Ne is a bicluster-like structure in the surface region but it could be more depressed in the internal region. This fact does not contradict with the conclusion in the proton-elastic scattering because a proton probe can only be sensitive to the surface region around the radius of the half density [50] and the internal region cannot directly be detected [72]. It leads to the interpretation that the shell-model-like configuration is favored in the internal region of the density distribution, while its surface region is dominated by the bicluster configuration. It is interesting to study the wave function that includes configuration mixing for unveiling detailed structure of ^{20}Ne. Also, we remark

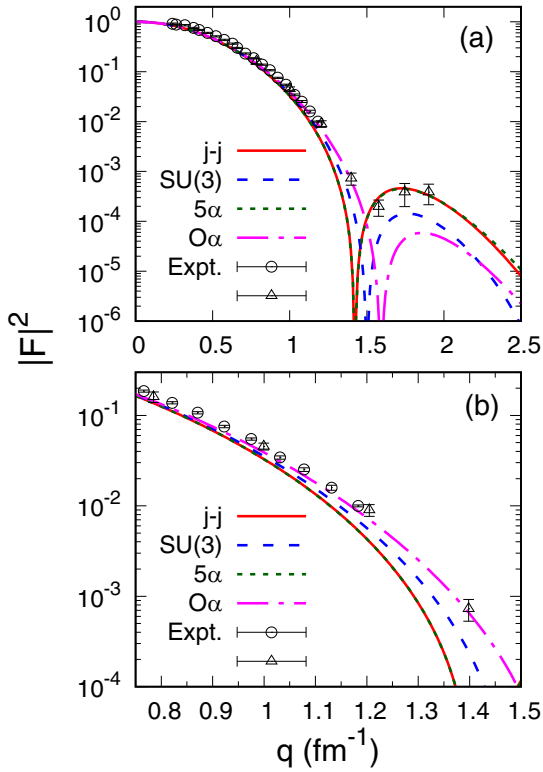

FIG. 5. Squared elastic charge form factors of ^{20}Ne. as a function of the momentum transfer in ranges of (a) [0:2.5] fm^{-1} and [0.75:1.5] fm^{-1}. The experimental data are taken from Refs. [19,83].

that the possibility of α cluster breaking in the internal region owing to the spin-orbit interaction was pointed out in Ref. [30], and recent α knockout reaction analysis showed that the spectroscopic factor of ^{16}O $+\alpha$ configuration is 0.26 in the ground state using the antisymmetrized molecular dynamics wave function [13], which is smaller than the cluster model prediction, 0.3–0.4 [84].

In the present analysis, we assume that the "^{16}O cluster" in ^{20}Ne has p-shell closed configuration. It seems to contradict with the fact that ^{16}O wave function in vacuum has the 4α tetrahedron configuration [16]. This can be explained as follows: The 4α tetrahedron configuration is not an ideal p-shell closed state but includes the mixture of sd shell but $1s$ orbit deficient [16]. We calculate the squared overlap between the tetrahedron 4α and p-shell configurations of ^{16}O and find that it is small, 0.024. Note that this value can be understood if the squared overlap between the Gaussian wave packets are 80% and evaluate $(0.8)^{16} = 0.03$. The overlap between the many-body wave functions is very sensitive to the shapes of the single-particle wave functions. The reason of this small squared overlap is partly because large intercluster distances d in the tetrahedron configuration and partly the difference in the ν parameters. For example, the squared overlap value is recovered to 0.12 ($\sim$88% for the average squared overlap of the Gaussian wave packets) when we take $d \to 0$ for the tetrahedron 4α configuration. In ^{20}Ne, an additional α particle

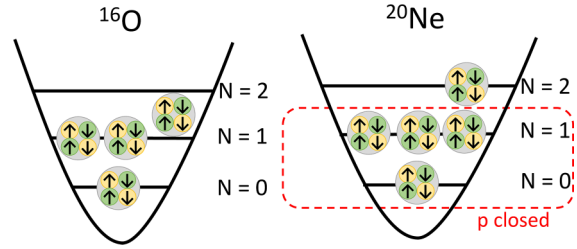

FIG. 6. Schematic picture of configurations of tetrahedron ^{16}O and bicluster ^{20}Ne configurations.

fills completely the p shell and partially the sd shell, and thus the p shell closed 16 nucleons plus α cluster structure is realized. A schematic picture is drawn in Fig. 6. From this interpretation, the Oα configuration should include a certain amount of the SU(3) configuration. In fact, the squared overlap between these configurations is large, 0.39.

IV. CONCLUSION

To explore the most probable configuration of the ground state of ^{20}Ne, we have made a comprehensive analysis by using various configurations generated from the antisymmetrized quasicluster model (AQCM). We have examined four AQCM configurations of the (a) j-j coupling and (b) SU(3) shell model, (c) 5α and (d) ^{16}O $+\alpha$-like cluster configurations. With these that reproduce the experimental charge radius data, we have calculated one-body density distributions and evaluated physical observables that directly reflect the characteristics of the density profiles.

We find that the characteristics of these four configurations are imprinted on the density profile near the nuclear surface, which can clearly be distinguished by comparing theoretical and experimental proton-nucleus elastic scattering cross sections. We conclude that the ground-state structure of ^{20}Ne includes a significant amount of a $16 + 4$ nucleon bicluster structure. We note, however, that the 16 nucleons do not necessarily mean ^{16}O in vacuum, i.e., 4α tetrahedron, but can be interpreted as the p-shell closed 16 nucleon configuration.

Also, the elastic charge form factor at high momentum region suggests that the breaking of the α cluster around ^{16}O may happen in the internal region of ^{20}Ne. The competition of j-j coupling shell model and α cluster structure and the relation to the spin-orbit interaction is an intriguing subject.

As an extension of the present study, exploring various cluster structure along heavier $N = Z$ nuclei such as ^{24}Mg, ^{28}Si, ^{32}S, and ^{36}Ar is interesting and will be reported elsewhere soon.

ACKNOWLEDGMENT

This work was in part supported by JSPS KAKENHI Grants No. 18K03635, No. 22H01214, and No. 22K03618.

[1] K. Ikeda, N. Takigawa, and H. Horiuchi, Prog. Theor. Phys. Suppl. **E68**, 464 (1968).
[2] K. Ikeda, H. Horiuchi, and S. Saito, Prog. Theor. Phys. Suppl. **68**, 1 (1980).
[3] Y. Fujiwara, H. Horiuchi, K. Ikeda, M. Kamimura, K. Katō, Y. Suzuki, and E. Uegaki, Prog. Theor. Phys. Suppl. **68**, 29 (1980).
[4] M. Freer, H. Horiuchi, Y. Kanada-En'yo, D. Lee, and U.-G. Meißner, Rev. Mod. Phys. **90**, 035004 (2018).
[5] F. Hoyle, Astrophys. J. Suppl. Series **1**, 121 (1955).
[6] R. J. deBoer, J. Görres, M. Wiescher, R. E. Azuma, A. Best, C. R. Brune, C. E. Fields, S. Jones, M. Pignatari, D. Sayre, K. Smith, F. X. Timmes, and E. Uberseder, Rev. Mod. Phys. **89**, 035007 (2017).
[7] M. Kamimura, Nucl. Phys. A **351**, 456 (1981).
[8] Y. Suzuki, Prog. Theor. Phys. **55**, 1751 (1976).
[9] Y. Suzuki, Prog. Theor. Phys. **56**, 111 (1976).
[10] A. Tohsaki, H. Horiuchi, P. Schuck, and G. Röpke, Phys. Rev. Lett. **87**, 192501 (2001).
[11] T. Wakasa, E. Ihara, K. Fujita, Y. Funaki, K. Hatanaka, H. Horiuchi, M. Itoh, J. Kamiya, G. Röpke, H. Sakaguchi *et al.*, Phys. Lett. B **653**, 173 (2007).
[12] S. Adachi, Y. Fujikawa, T. Kawabata, H. Akimune, T. Doi, T. Furuno, T. Harada, K. Inaba, S. Ishida, M. Itoh *et al.*, Phys. Lett. B **819**, 136411 (2021).
[13] K. Yoshida, Y. Chiba, M. Kimura, Y. Taniguchi, Y. Kanada-En'yo, and K. Ogata, Phys. Rev. C **100**, 044601 (2019).
[14] J. Tanaka, Z. H. Yang, S. Typel, S. Adachi, S. Bai, P. van Beek, D. Beaumel, Y. Fujikawa, J. Han, S. Heil *et al.*, Science **371**, 260 (2021).
[15] W. Horiuchi and N. Itagaki, Phys. Rev. C **106**, 044330 (2022).
[16] W. Horiuchi and N. Itagaki, Phys. Rev. C **107**, L021304 (2023).
[17] H. Horiuchi and K. Ikeda, Prog. Theor. Phys. **40**, 277 (1968).
[18] B. Zhou, Y. Funaki, H. Horiuchi, Z. Ren, G. Röpke, P. Schuck, A. Tohsaki, C. Xu, and T. Yamada, Phys. Rev. C **89**, 034319 (2014).
[19] Y. Horikawa, Phys. Lett. B **36**, 9 (1971).
[20] Y. Horikawa, Prog. Theor. Phys. **47**, 867 (1972).
[21] S. Hatakeyama and W. Horiuchi, Nucl. Phys. A **985**, 20 (2019).
[22] Y. Abgrall, P. Gabinski, and J. Labarsouque, Nucl. Phys. A **232**, 235 (1974).
[23] Y. Kanada-En'yo and H. Horiuchi, Prog. Theor. Phys. **93**, 115 (1995).
[24] M. Kimura, Phys. Rev. C **69**, 044319 (2004).
[25] P. Marević, J.-P. Ebran, E. Khan, T. Nikšić, and D. Vretenar, Phys. Rev. C **97**, 024334 (2018).
[26] E. Epelbaum, H. Krebs, T. A. Lähde, D. Lee, U.-G. Meißner, and G. Rupak, Phys. Rev. Lett. **112**, 102501 (2014).
[27] N. Itagaki, H. Masui, M. Ito, and S. Aoyama, Phys. Rev. C **71**, 064307 (2005).
[28] H. Masui and N. Itagaki, Phys. Rev. C **75**, 054309 (2007).
[29] T. Yoshida, N. Itagaki, and T. Otsuka, Phys. Rev. C **79**, 034308 (2009).
[30] N. Itagaki, J. Cseh, and M. Płoszajczak, Phys. Rev. C **83**, 014302 (2011).
[31] T. Suhara, N. Itagaki, J. Cseh, and M. Płoszajczak, Phys. Rev. C **87**, 054334 (2013).
[32] N. Itagaki, H. Matsuno, and T. Suhara, Prog. Theor. Exp. Phys. **2016**, 093D01 (2016).
[33] H. Matsuno, N. Itagaki, T. Ichikawa, Y. Yoshida, and Y. Kanada-En'yo, Prog. Theor. Exp. Phys. **2017**, 063D01 (2017).
[34] H. Matsuno and N. Itagaki, Prog. Theor. Exp. Phys. **2017**, 123D05 (2017).
[35] N. Itagaki, Phys. Rev. C **94**, 064324 (2016).
[36] N. Itagaki and A. Tohsaki, Phys. Rev. C **97**, 014307 (2018).
[37] N. Itagaki, H. Matsuno, and A. Tohsaki, Phys. Rev. C **98**, 044306 (2018).
[38] N. Itagaki, A. V. Afanasjev, and D. Ray, Phys. Rev. C **101**, 034304 (2020).
[39] N. Itagaki, T. Fukui, J. Tanaka, and Y. Kikuchi, Phys. Rev. C **102**, 024332 (2020).
[40] N. Itagaki and T. Naito, Phys. Rev. C **103**, 044303 (2021).
[41] D. M. Brink, Many-body description of nuclear structure and reactions, in *Proceedings of the International School of Physics "Enrico Fermi"*, Course XXXVI, edited by L. Bloch (Academic Press, New York, 1966), p. 247.
[42] W. Horiuchi, Y. Suzuki, B. Abu-Ibrahim, and A. Kohama, Phys. Rev. C **75**, 044607 (2007); **76**, 039903(E) (2007).
[43] W. Horiuchi, T. Inakura, T. Nakatsukasa, and Y. Suzuki, Phys. Rev. C **86**, 024614 (2012).
[44] R. J. Glauber, in *Lectures in Theoretical Physics*, edited by W. E. Brittin and L. G. Dunham (Interscience, New York, 1959), Vol. 1, p. 315.
[45] Y. Suzuki, R. G. Lovas, K. Yabana, and K. Varga, *Structure and Reactions of Light Exotic Nuclei* (Taylor & Francis, London, 2003).
[46] L. Ray, Phys. Rev. C **20**, 1857 (1979).
[47] B. Abu-Ibrahim, W. Horiuchi, A. Kohama, and Y. Suzuki, Phys. Rev. C **77**, 034607 (2008); **80**, 029903(E) (2009); **81**, 019901(E) (2010).
[48] B. Abu-Ibrahim, S. Iwasaki, W. Horiuchi, A. Kohama, and Y. Suzuki, J. Phys. Soc. Jpn. **78**, 044201 (2009).
[49] W. Horiuchi, S. Hatakeyama, S. Ebata, and Y. Suzuki, Phys. Rev. C **93**, 044611 (2016).
[50] S. Hatakeyama, W. Horiuchi, and A. Kohama, Phys. Rev. C **97**, 054607 (2018).
[51] B. Abu-Ibrahim and Y. Suzuki, Phys. Rev. C **61**, 051601(R) (2000).
[52] W. Horiuchi, Y. Suzuki, and T. Inakura, Phys. Rev. C **89**, 011601(R) (2014).
[53] K. Makiguchi and W. Horiuchi, Prog. Theor. Exp. Phys. **2022**, 073D01 (2022).
[54] R. Kanungo, A. Prochazka, W. Horiuchi, C. Nociforo, T. Aumann, D. Boutin, D. Cortina-Gil, B. Davids, M. Diakaki, F. Farinon *et al.*, Phys. Rev. C **83**, 021302(R) (2011).
[55] R. Kanungo, A. Prochazka, M. Uchida, W. Horiuchi, G. Hagen, T. Papenbrock, C. Nociforo, T. Aumann, D. Boutin, D. Cortina-Gil *et al.*, Phys. Rev. C **84**, 061304(R) (2011).
[56] S. Bagchi, R. Kanungo, Y. K. Tanaka, H. Geissel, P. Doornenbal, W. Horiuchi, G. Hagen, T. Suzuki, N. Tsunoda, D. S. Ahn *et al.*, Phys. Rev. Lett. **124**, 222504 (2020).
[57] W. Horiuchi and Y. Suzuki, Phys. Rev. C **74**, 034311 (2006).
[58] W. Horiuchi, Y. Suzuki, P. Capel, and D. Baye, Phys. Rev. C **81**, 024606 (2010).
[59] W. Horiuchi, T. Inakura, T. Nakatsukasa, and Y. Suzuki, JPS Conf. Proc. **6**, 030079 (2015).
[60] T. Nagahisa and W. Horiuchi, Phys. Rev. C **97**, 054614 (2018).
[61] I. Angeli and K. P. Marinova, At. Data Nucl. Data Tables **99**, 69 (2013).

[62] Y. Suzuki, K. Arai, Y. Ogawa, and K. Varga, Phys. Rev. C **54**, 2073 (1996).
[63] T. Neff, J. Phys.: Conf. Ser. **403**, 012028 (2012).
[64] W. Horiuchi and Y. Suzuki, Phys. Rev. C **89**, 011304(R) (2014).
[65] W. Horiuchi and Y. Suzuki, Phys. Rev. C **90**, 034001 (2014).
[66] S. Kox, A. Gamp, C. Perrin, J. Arvieux, R. Bertholet, J. F. Bruandet, M. Buenerd, R. Cherkaoui, A. J. Cole, Y. El-Masri *et al.*, Phys. Rev. C **35**, 1678 (1987).
[67] L. Chulkov, G. Kraus, O. Bochkarev, P. Egelhof, H. Geissel, M. Golovkov, H. Irnich, Z. Janas, H. Keller, T. Kobayashi *et al.*, Nucl. Phys. A **603**, 219 (1996).
[68] M. Takechi, T. Ohtsubo, M. Fukuda, D. Nishimura, T. Kuboki, T. Kubo, T. Suzuki, T. Yamaguchi, A. Ozawa, T. Moriguchi, and H. Ooishi, Phys. Lett. B **707**, 357 (2012).
[69] A. Kohama, K. Iida, and K. Oyamatsu, Phys. Rev. C **78**, 061601(R) (2008).
[70] W. Horiuchi and T. Inakura, Prog. Theor. Exp. Phys. **2021**, 103D02 (2021).
[71] T. Dytrych, K. D. Launey, J. P. Draayer, D. J. Rowe, J. L. Wood, G. Rosensteel, C. Bahri, D. Langr, and R. B. Baker, Phys. Rev. Lett. **124**, 042501 (2020).
[72] V. Choudhary, W. Horiuchi, M. Kimura, and R. Chatterjee, Phys. Rev. C **102**, 034619 (2020).
[73] V. Choudhary, W. Horiuchi, M. Kimura, and R. Chatterjee, Phys. Rev. C **104**, 054313 (2021).
[74] W. Horiuchi, T. Inakura, and S. Michimasa, Phys. Rev. C **105**, 014316 (2022).
[75] W. Horiuchi, T. Inakura, S. Michimasa, and M. Tanaka, Phys. Rev. C **107**, L041304 (2023).
[76] M. Tanaka, M. Takechi, M. Fukuda, D. Nishimura, T. Suzuki, Y. Tanaka, T. Moriguchi, D. S. Ahn, A. Aimaganbetov, M. Amano *et al.*, Phys. Rev. Lett. **124**, 102501 (2020).
[77] W. Horiuchi, Prog. Theor. Exp. Phys. **2021**, 123D01 (2021).
[78] W. Horiuchi and T. Inakura, Phys. Rev. C **105**, 044303 (2022).
[79] G. S. Blanpied, B. G. Ritchie, M. L. Barlett, R. W. Fergerson, G. W. Hoffmann, J. A. McGill, and B. H. Wildenthal, Phys. Rev. C **38**, 2180 (1988).
[80] R. P. Singhal, H. S. Caplan, J. R. Moreira, and T. E. Drake, Can. J. Phys. **51**, 2125 (1973).
[81] B. Pritychenko, M. Birch, B. Singh, and M. Horoi, At. Data Nucl. Data Tables **107**, 1 (2016).
[82] R. Hofstadter, Rev. Mod. Phys. **28**, 214 (1956).
[83] E. A. Knight, R. P. Singhal, R. G. Arthur, and M. W. S. Macauley, J. Phys. G: Nucl. Phys. **7**, 1115 (1981).
[84] F. Nemoto, Y. Yamamoto, H. Horiuchi, Y. Suzuki, and K. Ikeda, Prog. Theor. Phys. **54**, 104 (1975).